



## OPEN Nickel silicide nanowire anodes for microbial fuel cells to advance power production and charge transfer efficiency in 3D configurations

Mohammad Hosseini<sup>1,2</sup>, S. Ahmad Etghani<sup>1,2,3</sup>, Mir Razi Mousavi<sup>4</sup>, Mahdieh Joharifar<sup>1</sup>, Mehdi Akbari<sup>1</sup>, Zeinab Sanaee<sup>4</sup> & Shams Mohajerzadeh<sup>1</sup>✉

The growing energy demands of the industrial world have driven advancements in green energy technologies. Microbial fuel cells (MFCs), which harness power from microorganisms, show promise for energy extraction from wastewater and sludge. However, challenges remain in improving power output and sustaining performance under high-charge conditions. Incorporating nanomaterials into 3D structures offers potential solutions, including miniaturized designs. This study introduces nickel silicide nanowires as anode materials for MFCs. Synthesized on nickel foam, these nanowires form a 3D nickel-based structure with semi-metal nanostructures. Tested in a microfluidic MFC system with *E. coli*, this configuration achieved significant improvements, including a peak power density of 323 mW m<sup>-2</sup> and a current density of 2.24 A m<sup>-2</sup>, representing a 2.5-fold increase in power and a 4-fold boost in current compared to bare nickel foam. Nutrient broth proved the most effective charge transfer medium, surpassing glucose and urea by 3 and 5 times, respectively. These results, supported by EIS and SEM analyses, highlight the role of nanowires in enhancing charge transfer and sustaining high-current performance. The presented 3D nickel-based configuration anode offers advancements in microbial fuel cell technology, providing a foundation for further enhancements and applications in energy harvesting systems.

**Keywords** Nickel silicide nanowire, Microbial fuel cell, Microfluidics, 3D anodes

Microbial fuel cells (MFCs) have emerged as a promising platform for clean energy harvesting, generating electricity from biodegradable organic materials through the metabolic processes of microorganisms. The development of MFC technologies over the past decade has led to a range of applications, including hydrogen generation<sup>1</sup>, desalination<sup>2</sup>, wastewater treatment<sup>3</sup>, and sensing<sup>4</sup>. Additionally, integrating microfluidics with MFCs can enhance their performance and expand their applications<sup>5</sup>. Micro-scale MFCs provide an on-chip power source suitable for microscale sensors, portable electronics, and implantable medical devices<sup>6</sup>. However, factors such as low power density and stability limit their practical applications<sup>7</sup>. While the performance of MFCs can be influenced by various factors, including cell design and the materials used for the anode and cathode, the anode material and structure play a pivotal role in overall cell performance, particularly in extracellular electron transfer between the anode and the biofilm<sup>8</sup>. The materials must exhibit excellent conductivity, biocompatibility, chemical stability, catalytic activity, and cost-effectiveness to enhance the efficiency and effectiveness of the MFC electrode<sup>9</sup>. Utilizing a 3D structure and modifying the electrode with nanostructures to increase the accessible surface area can significantly enhance the power density of MFCs. A porous anode structure enables internal colonization and fosters strong interactions between the anode and biofilms<sup>10</sup>. Researchers have experimented with various materials for anode electrodes, such as carbon cloth<sup>11</sup>, carbon foam<sup>12</sup>, nickel foam<sup>13</sup>, and steel foam<sup>14</sup>. Additionally, nanostructures like FeS<sub>2</sub> nanoparticles<sup>15</sup>, graphene<sup>16</sup>, nanofibers<sup>17</sup>, carbon nanotubes<sup>18</sup>,

<sup>1</sup>Thin Film and Nano-Electronic Lab, School of Electrical and Computer Eng, University of Tehran, Tehran 14395-515, Iran. <sup>2</sup>Condensed Matter National Laboratory, Institute for Research in Fundamental Sciences, Tehran 19395-5531, Iran. <sup>3</sup>School of Biological Sciences, Institute for Research in Fundamental Sciences, Tehran 19395-5746, Iran. <sup>4</sup>Nano-Fabricated Energy Devices Lab, School of Electrical and Computer Eng, University of Tehran, Tehran 14395-515, Iran. ✉email: mohajer@ut.ac.ir

and 3D chitosan-carbon nanotube scaffolds<sup>19</sup> electrodes have been used to enhance MFC performance. Carbon and its composites are among the most extensively studied anode materials in microbial fuel cells<sup>20</sup>. While some exhibit high performance, their use is often limited by factors such as small surface area, restricted bacterial adhesion, high production costs, and the need for additional conductivity enhancements<sup>21,22</sup>. These challenges have been addressed through various anode modification techniques, including the incorporation of conductive polymers, carbon composites, and metallic compounds<sup>23</sup>. Metallic anodes present an alternative for hosting electroactive bacteria due to their distinct physical and chemical properties<sup>24,25</sup>. However, smooth metal surfaces hinder bacterial adhesion, reducing efficiency<sup>26,27</sup>. Additionally, electrode corrosion in metals limits their long-term use as anode materials. Even non-corrosive metals like stainless steel suffer from irreversible electron transfer due to the formation of passivating oxidation layers<sup>28</sup>. While noble metals such as gold and platinum offer advantages, their high cost makes them impractical for large-scale applications<sup>29</sup>. To overcome these challenges, incorporating porous materials with nanostructured surfaces can enhance surface area and bacterial adhesion. Furthermore, metal silicides have emerged as promising candidates for MFC anodes, offering improved stability and performance by mitigating corrosion-related issues.

Transition metal silicides have been widely used in microelectronics and nanoelectronics devices due to their properties, including high melting point, high resistance to oxidation and corrosion, high electrical conductivity, and narrow band gap<sup>30–32</sup>. One-dimensional (1D) transition metal silicides have been synthesized and applied in various electronic, photonic, and other functional devices<sup>33,34</sup>. Among these, nickel silicide nanowires are particularly noteworthy due to their high conductivity and growth temperature<sup>35,36</sup>. Various methods have been employed to grow 1D silicides, including chemical vapor deposition (CVD)<sup>37,38</sup>, chemical vapor transport (CVT)<sup>39</sup>, silicidation of silicon nanowires<sup>40</sup>, and metal-induced growth<sup>41</sup>, reflecting their wide range of applications. The CVD growth of nickel silicide nanowires is widely used due to its ability to form single-crystalline structures, and the growth process can be easily integrated with silicon processing technology.

Nickel is a key material widely used in energy storage devices due to its high conductivity, oxidation resistance, and large surface area<sup>42,43</sup>. Nickel foam, in particular, has been employed as a substrate in energy storage applications and is frequently utilized as an anode in microbial fuel cells. To improve the performance of nickel-based anodes, various modification strategies have been explored<sup>5</sup>. Some research groups have incorporated graphene or nickel nanoparticles into nickel foam or nickel foil to enhance conductivity and bacterial adhesion<sup>44–46</sup>. While graphene-based modifications have successfully boosted MFC performance, they also introduce challenges such as increased production costs, biocompatibility concerns, and limited repeatability<sup>47–49</sup>.

In this study, we report the fabrication of an MFC anode using nickel foam enhanced with nickel silicide nanowires to increase surface area. A novel method for growing nickel silicide nanowires on nickel foam was developed to improve surface area and promote bacterial colonization. This high-performance MFC anode, utilizing nickel foam as a 3D conducting scaffold with nickel silicide nanowires, significantly increased power density in microfluidic MFCs. The semi-metallic nature of nickel silicide facilitates efficient electron transfer to the external circuit. Additionally, the 3D scaffold formed by coating nickel foam with nanostructures provides an effective strategy for minimizing mass transport limitations while enhancing microbial colonization and biofilm formation, ultimately improving MFC efficiency. The nickel-based anodes, with their large pores, prevent bacterial entrapment, allowing for free nutrient flow and enhanced microorganism growth. Additionally, the silicide nanowires further increase the surface area, promoting better bacterial interaction with the electrode. Consequently, a new high-performance, low-cost microfluidic device was fabricated and characterized based on cell potential evolution, polarization curves, anode electrode morphology, and various operational modes. Furthermore, the effects of different substrates, including nutrient broth, glucose, and urea, were investigated and compared against one another. Overall, this design addresses common limitations in microbial fuel cells, resulting in improved performance.

## Materials and methods

### Cathode fabrication

For cathode preparation, carbon cloth was coated with a slurry composed of a carbon platinum catalyst (10 wt% Pt/C, Merck, 0.5 mg per 1 cm<sup>2</sup> of carbon cloth), Nafion solution (5% Alfa Aesar, 7  $\mu$ L per 1 mg of Pt/C), and isopropanol (Merck, 3.3  $\mu$ L per 1 mg of Pt/C). The coated cathode was then dried at 80 °C for approximately 20 min, as described in other studies.

### Characterization

The morphology of the samples was characterized using a Hitachi S4160 field-emission scanning electron microscope (FESEM) equipped with an EDAX energy-dispersive X-ray analyzer. Electrochemical impedance spectroscopy (EIS) tests were performed with a Metrohm DropSens  $\mu$ Stat-I 400s. For these tests, small sealed channels were incorporated into the top of the microfluidic device to act as counter and reference electrodes. Ag/AgCl paste was applied to the reference electrode, while the anode served as the working electrode. To simulate the results and determine the optimal equivalent circuit, IviumSoft software (Ivium Technologies) was utilized.

### Microbial culture

*Escherichia coli* ATCC-11,105 was obtained from the Biochemical and Bioenvironmental Research Center of Sharif University of Technology for this study. The bacteria were cultured in nutrient broth (NB) medium, comprising 1 g of beef extract, 2 g of yeast extract, 5 g of peptone, and 5 g of NaCl per liter, under shaking conditions (150 rpm) at 37 °C for approximately 48 h. Throughout the startup and enrichment periods, the open circuit potential (OCP) was measured to confirm the formation of a homogeneous and uniform biofilm.

### Microbial fuel cell assembly

A single-chamber microfluidic setup was employed to evaluate the potential of the as-prepared nanomaterial for sustainable energy harvesting. The microchannel dimensions were 8 mm in width, 12 mm in length, and 300  $\mu\text{m}$  in height. The microchannel was fabricated by laser cutting polymethyl methacrylate (PMMA). Both the anode and cathode electrodes measured 8 mm  $\times$  8 mm. The anodic PMMA plate was engraved to create the electrode placement site for the anode, forming the reaction chamber. A via was drilled to enable connection of the anode electrode to the external circuit, while a window was created on the cathode to expose the carbon cloth to air and facilitate its contact with the external circuit. The anode and cathode electrodes were connected to the external circuit using silver conductive paste. The PMMA plates were drilled to create the inlet and outlet pathways. A 300  $\mu\text{m}$ -thick polyethylene terephthalate (PET) sheet was patterned and inserted between the two PMMA plates to precisely control the spacing between the electrodes. These plates were then bonded using double-sided adhesive tapes. The entire assembly was held together with four screws and nuts, and the chamber was sealed with an O-ring to ensure a tight closure.

### Microbial fuel cell operation and measurements

Under open-circuit conditions, with continuous monitoring of the cell's potential, a fed-batch approach was employed to initialize cell performance through sequential refreshment of the microbial medium by injecting *E. coli* microorganisms and nutrients. A custom-built readout circuit was designed for data logging. The cell's performance was evaluated by switching resistive loads, controlled via a programmable interface circuit. A range of resistive loads, from 680  $\Omega$  to 220 k $\Omega$ , was applied to assess the cell's power production capabilities. The operation of the cell was further examined under varying nutrient-feeding rates. To ensure a consistent nutrient supply for the microorganisms, the substrate was injected into the cell using a syringe pump with adjustable and steady flow rates.

## Results and discussion

### Growth of nickel silicide nanowires on nickel foam

The nickel foam (99.99% purity) of size 8  $\times$  8 mm was cleaned in an ultrasonic bath containing acetone, followed by rinsing with diluted HCl solution and ethanol. Nickel silicide nanostructures were synthesized using a low-pressure home-made chemical vapor deposition system (LPCVD) in a horizontal tube furnace operating at 10 mTorr to 10 Torr pressures. The sample was positioned in the center of the furnace and heated to 600  $^{\circ}\text{C}$  in an argon gas environment. Once the temperature reached 600  $^{\circ}\text{C}$ ,  $\text{SiH}_4$  (50 sccm) and argon gas (50 sccm) were introduced into the chamber for 120 s. After the reaction time, the sample was cooled to room temperature under argon gas. Upon removal from the chamber, the surface color of the foam changed to black. The scanning electron microscopy image of the nickel foam surface after the synthesis process is presented in Fig. 1a. In addition, Fig. 1b displays SEM image of the nickel foam before the synthesis process.

The SEM image reveals grain boundaries on the surface of the nickel foam, which significantly influence the morphology of the nickel silicide nanostructures. Specifically, the SEM image of the synthesized nanostructures (Fig. 1c) shows that cone-shaped nanostructures uniformly cover the surface. This growth method is advantageous due to its simplicity, ability to conform to complex surfaces, and potential for large-area growth with high reproducibility.

The phase diagram of the nickel-silicon system indicates that the eutectic temperature of the nickel-silicon phases exceeds 800  $^{\circ}\text{C}$ , which means the traditional vapor-liquid-solid (VLS) growth mechanism cannot account for the formation of these nanostructures<sup>35</sup>. Instead, the growth mechanism of nickel silicide is driven by the decomposition of  $\text{SiH}_4$  and the diffusion of nickel atoms into the silicon layer that forms on the surface of the nickel foam. The catalytic decomposition of  $\text{SiH}_4$  on the nickel surface enables growth at relatively low temperatures.  $\text{SiH}_4$  decomposes in the presence of heat, typically above 300  $^{\circ}\text{C}$ , to form silicon atoms, hydrogen gas, and silicon radicals<sup>35,50</sup>. As  $\text{SiH}_4$  decomposes, a thin silicon layer is deposited onto the nickel foam surface<sup>51</sup>.

The silicon atoms then interact with the nickel, forming a silicon-rich layer. Studies indicate that nickel is the fastest diffusing element in silicon<sup>52</sup>, accelerating the diffusion of nickel atoms into the silicon layer, where they react to form nickel silicide<sup>53</sup>. This process continues until a stable nickel silicide layer forms, contributing to the growth of the nanostructures. The grain boundaries in the nickel foam play a crucial role in the formation of these nickel silicide layers. During nanostructure growth, the diffusion of nickel atoms toward the upper regions of the structures decreases, causing the diameter of these structures to become smaller and resulting in the formation of cone-shaped nanostructures on the surface of the nickel foam grains.

In this study, the growth of cone-shaped nanostructures was modified to facilitate the growth of nickel silicide nanowires. To achieve this, we divided our synthesis process into two distinct stages. Initially, before introducing  $\text{SiH}_4$  into the chamber, a grain modification step was employed. This step involved introducing  $\text{SiH}_4$  (50 sccm) along with a mixture of ammonia (<2.0%) and argon gas (50 sccm) into the chamber for 120 s. This grain modification step regulates the shapes of the grains, creating conditions conducive to the growth of nickel silicide nanowires. During this process, nickel acts as a catalyst for ammonia<sup>54</sup>, decomposing it into nitrogen and hydrogen. The presence of nitrogen atoms near the surface of the nickel foam can lead to the formation of  $\text{SiN}_x$  in the presence of  $\text{SiH}_4$ . Due to the limited concentration of nitrogen atoms, a uniform layer of  $\text{SiN}_x$  does not form; rather, it confines the formation of the nickel silicide layer. The use of  $\text{SiN}_x$  modifies the morphology of the grains, limits the growth of large nickel silicide particles, and confines nucleation, which promotes the one-dimensional growth of nickel silicide nanostructures. This modification facilitates the subsequent growth of nickel silicide nanowires, as illustrated in Fig. 1d and e. The diameter of the nickel silicide nanowires is less than 100 nm, with a length of approximately 5  $\mu\text{m}$ . Energy Dispersive Spectroscopy (EDS) of the nickel silicide nanowires, shown in Fig. 1f, confirms the presence of Ni and Si atoms, indicating the diffusion of nickel atoms into the nanowires. The EDS mapping analysis in Fig. 1g examines the existence of other atomic compounds

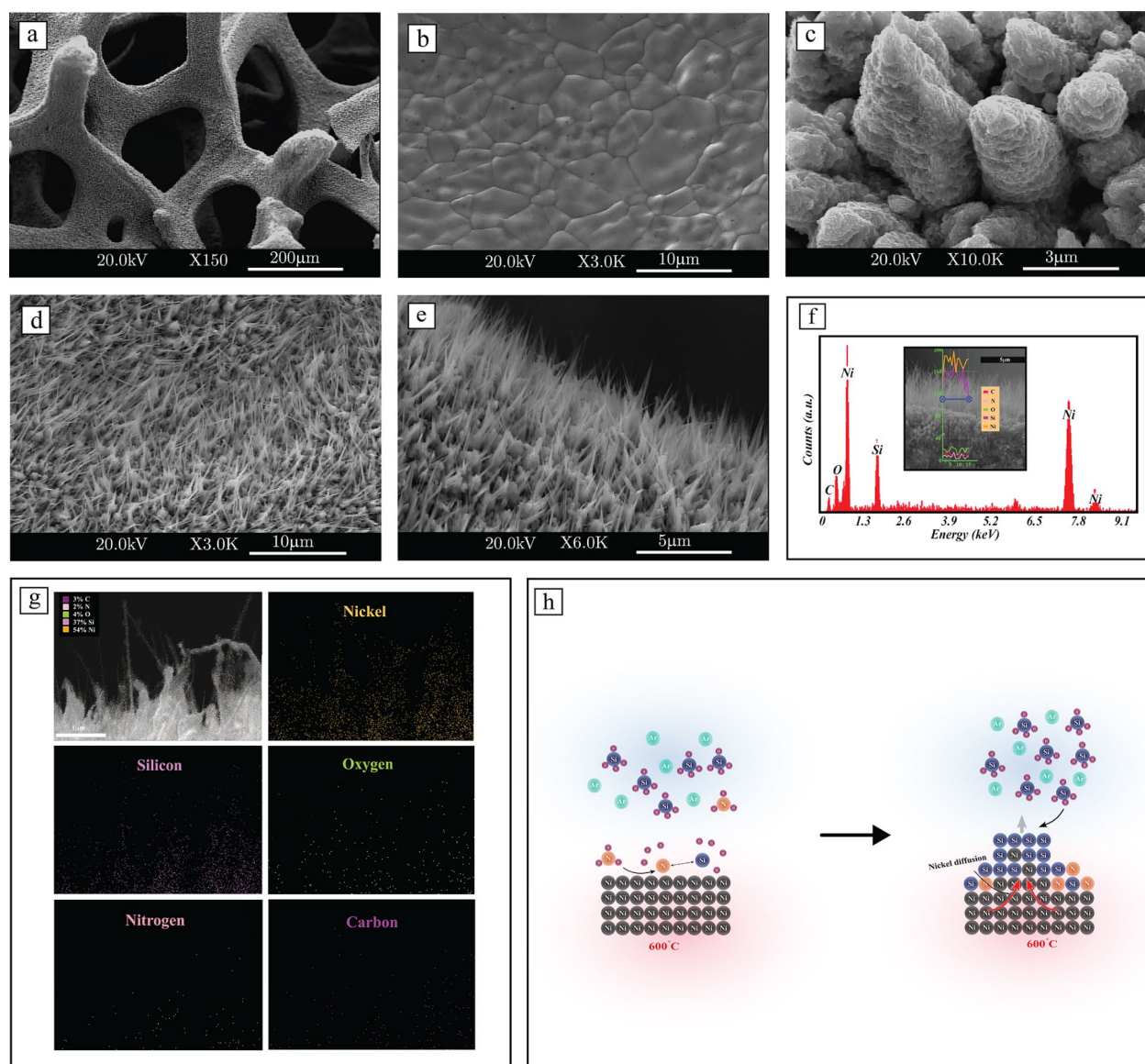


**Fig. 1.** SEM images of nickel silicide nanowires and their growth mechanism. **(a)** Low magnification SEM image of nickel silicide nanowires on the surface of nickel foam. **(b)** SEM image showing the grain boundaries of nickel foam before the growth process, where grains act as growth regions, leading to the formation of cone-shaped structures. **(c)** SEM image of cone-shaped structure growth on the foam substrate in the absence of  $\text{NH}_3$  gas. **(d)** and **(e)** SEM images of the uniform growth of nickel silicide nanowires on the surface of nickel foam. **(f)** EDS analysis of nickel silicide nanowires shows that the nanowires are composed of silicon and nickel. (Inset: Line scan EDS analysis of nanowires confirms the presence of nickel and silicon atoms.) **(g)** EDS map analysis of nickel silicide nanowire. **(h)** Schematic of the growth process of nickel silicide. The decomposition of silane and ammonia on the foam surface modifies the grain shapes. The presence of nitrogen and silicon atoms near the surface of the nickel foam can lead to the formation of  $\text{SiN}_x$ , a crucial step for the subsequent growth of nickel silicide nanowires.

present during the synthesis process and confirms the predominant role of nickel and silicon atoms. Figure 1h schematically illustrates the process of nickel silicide nanowire synthesis as described.

### Microbial fuel cell

#### *Nickel silicide nanowires and nickel foam as anode electrodes*

Microfluidic architectures in MFCs offer a promising approach to enhancing performance and scalability. Additionally, incorporating nanostructures into fuel cell electrodes increases surface power density by providing a larger effective surface area. In this study, we utilized the as-prepared structures and nickel foam as an anode material in microfluidic-based microbial fuel cells. (Fig. 2)



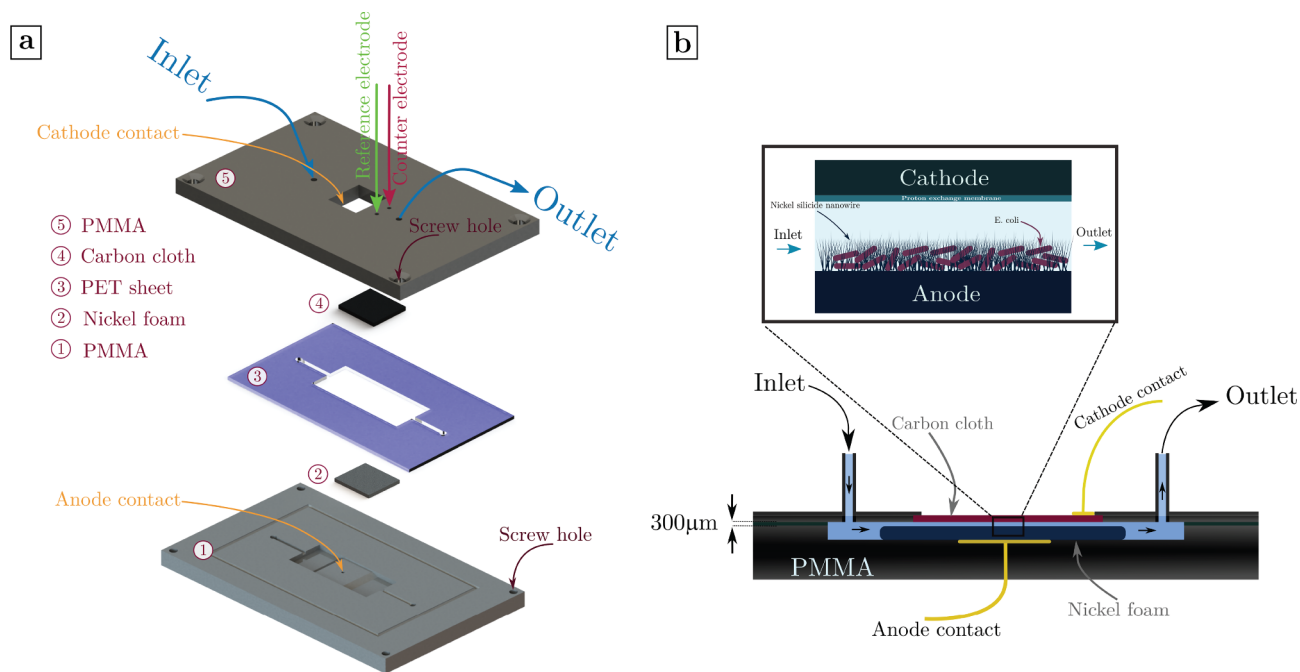


**Fig. 2.** Schematic details of the microfluidic-based microbial fuel cell. **(a)** Exploded view of the PMMA microfluidic structure. Nickel foam is used as the anode, and carbon cloth serves as the cathode electrode. Both the anode and cathode have a surface area of  $8 \times 8$  mm. A PMMA sheet with a thickness of  $300 \mu\text{m}$  is utilized as the separator. The microchannel dimensions are  $8$  mm in width and  $12$  mm in length. The microfluidic cell is encapsulated by two channel-engraved PMMA sheets bonded together. **(b)** cross-sectional view of Microfluidic-based Microbial Fuel cell. The inlet and outlet serve as the paths for introducing the microorganism and microbial substrate.

To investigate the capabilities of nickel silicide nanowires in energy acquisition, nickel foam covered with these nanowires (Ni-W) was compared with bare nickel foam (Ni-F) as an anode electrode in single-chamber microfluidic microbial fuel cells. Microbial inoculation was performed in fed-batch mode. To achieve a uniform and effective biofilm formation, the startup process operated under OCP conditions<sup>55</sup>. This process involved injecting NB-enriched *E. coli* into the MFC and continuously monitoring OCP until a sustainable condition was reached. During batch mode operation, fresh medium was supplied whenever a drop in OCP was observed. A saturation of about  $600$  mV in OCP was obtained for the microfluidic MFC, indicating stable biocatalyst activity and successful bacterial enrichment, as evidenced by minor variations in the OCP value. Although the colonization of microorganisms on the Ni-F surface shows a non-uniform formation, as depicted in Fig. 3a and b, the SEM images in Fig. 3c and d reveal a uniform microbial community formation on the Ni-W surface. The colonization of microorganisms on the surface and dense biofilm formation wrapped in matrices on the electrode suggest enhanced current density. The vertical growth orientation of silicide nanowires on nickel foam presents a 3D structure desirable for bacterial inhabitation. In regions with a sparse bacterial community (Fig. 3e and f), the electroactive matrices cover these nanowires and provide an electron pathway to the underlying nickel foam substrate. Also, rod-shaped bacteria have the opportunity to form on these vertically oriented structures. The higher surface area provided by nanostructures has resulted in an efficient microbial community. Despite the dense, layered film established on the electrode, it has suppressed bacterial aggregation, preventing microorganism death. Clogging in the pores of porous materials, which leads to bacterial entrapment and subsequent cell death, has been a limitation in 3D structures, reducing the active surface of the electrode for current acquisition<sup>56</sup>. The nickel-based anodes employed in the fabricated cells are comprised of nickel foams with pore sizes as high as  $500 \mu\text{m}$ , which do not constrain bacteria and nutrient feeding. Additionally, the anchored foams with silicide nanowires provide a higher surface area favorable for microorganism growth and metabolism. Due to the semi-metal nature of nickel silicide, electron transfer from inoculated bacteria to the nickel substrate is facilitated, leading to higher power generation in the cell.

The performance evaluation of two microbial fuel cells (Ni-W and Ni-F) was assessed with different external loads to investigate their power generation capability. Voltage drops across varying external resistors, ranging from  $680 \Omega$  to  $220 \text{k}\Omega$ , were recorded. These measurements were conducted under various substrate flow rates to determine the optimal feeding rate in continuous mode. The variation in substrate delivery to the electrodes, influenced by the fluid dynamics in the microfluidic chamber, along with the need to provide sufficient time for nutrient transport to the biofilm and subsequent bacterial metabolism, necessitates flow rate optimization in microfluidic MFCs. Moreover, the substrate flow rate plays a crucial role in the power density of microbial fuel cells<sup>57</sup>. While a high flow rate increases mass transfer between the biofilm and substrate, potentially enhancing microbial activity and electron production, it may also reduce the substrate's retention time. Studies show that

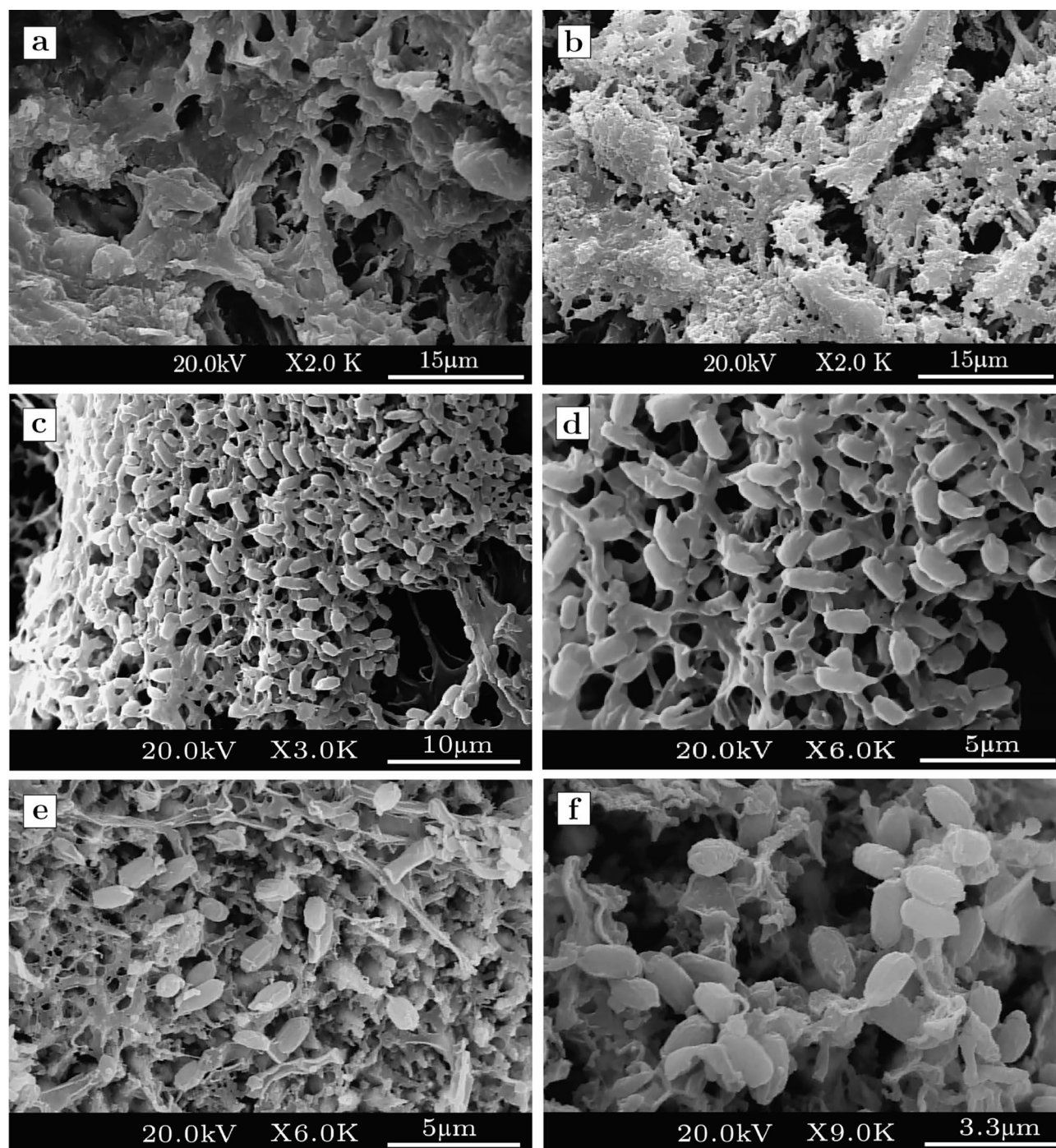


**Fig. 3.** Formation of biofilm on the Ni-F and Ni-W anode electrode. (a) and (b) The non-uniform formation of bacterial communities on the Ni-F electrode (c) and (d) Uniform colonization of bacterial communities on the nanostructure-coated nickel foam surface in the Ni-W electrode. The presence of microorganisms within the uniform bacterial matrix facilitates electron transfer. (e) and (f) The electroactive biofilm layer covering the nickel silicide nanowire structures. The formation of these matrices over the semi-metal nanostructures provides pathways from the *E. coli* surface to the anode electrode, enhancing the cell's charge transfer capability.

excessive flow rates can lead to hydrodynamic instability, causing fluctuations in the flow streams<sup>58,59</sup>. This instability may result in irregular widening or narrowing, which can cause contact with the opposite electrode in a microfluidic system. It can also shear off biofilms and reduce active microbial populations<sup>60</sup>. These factors have adverse impacts on fuel cell performance.

The surface power density curves of the Ni-F and Ni-W anodes, presented in Fig. 4a and d respectively, demonstrate an optimal flow rate of  $4 \mu\text{l min}^{-1}$  for both cells. The occurrence of maximum power at this

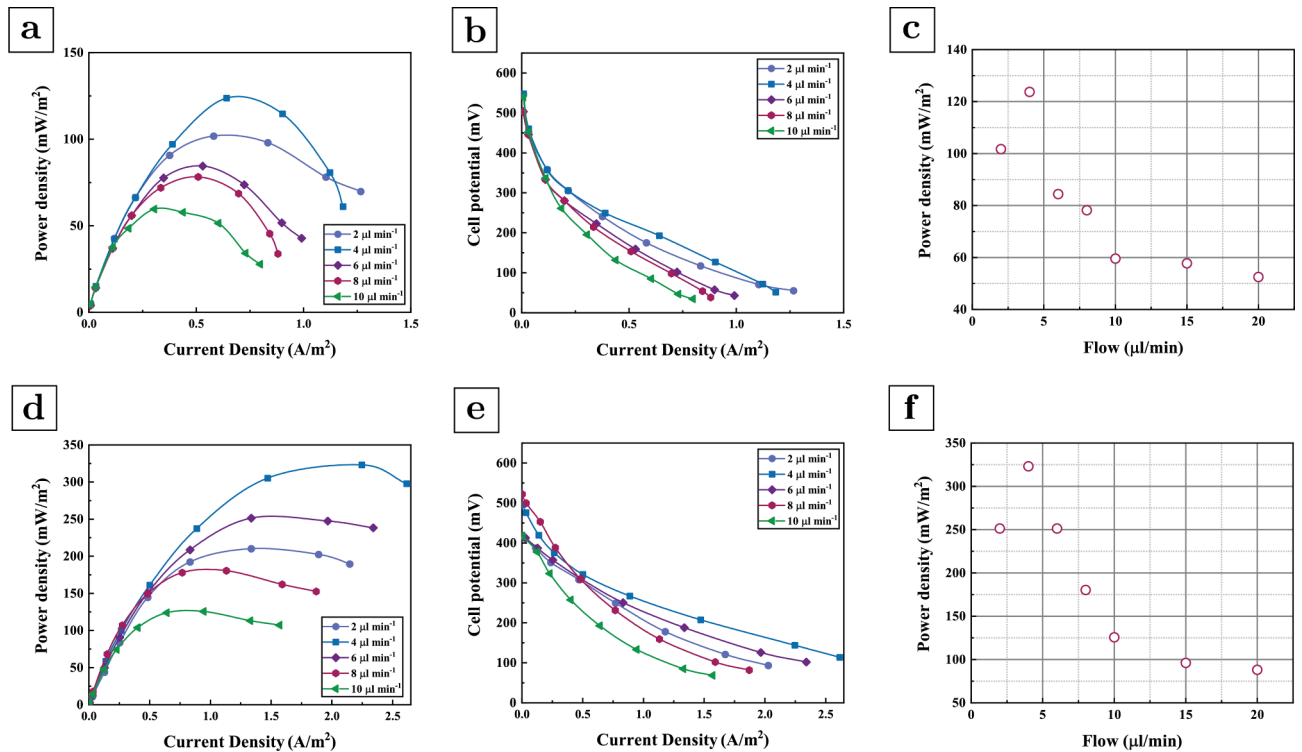


**Fig. 4.** Effect of nanostructure and flow rate on microfluidic fuel cell responses. **(a)** Surface power density of the nickel foam anode at various flow rates. **(b)** Polarization curves of the nickel foam anode at various flow rates. **(c)** Maximum surface power density of the nickel foam anode at various flow rates. **(d)** Surface power density of the nickel nanowires on the foam anode at various flow rates. **(e)** Polarization curves of the nickel nanowire on the foam anode at various flow rates. **(f)** Maximum surface power density of the nickel nanowire on the foam anode at various flow rates.

flow rate for both cells (depicted in Fig. 4c and f) indicates the establishment of hydrodynamic conditions at the optimal point. Comparing the power generation efficiency of bare nickel foam with foams covered with nanostructures highlights the advantages brought by nanowires. While the maximum surface power density of Ni-F is approximately  $125 \text{ mW m}^{-2}$ , the Ni-W anode shows a 2.5-fold enhancement in power generation, reaching up to  $323 \text{ mW m}^{-2}$  at the maximum point. On the other hand, although the Ni-F anode experiences a distinguishable peak in power density followed by performance degradation at higher current densities due to its inability to efficiently acquire electrons from the microorganism metabolic cycle, the Ni-W anode exhibits remarkable sustainability at higher current densities. The 7% variation in power density in the range of 1.5 to  $2.7 \text{ A m}^{-2}$  depicts the anode's endurance under the higher current supply. This persistent power production capability at higher current densities broadens the operational range of the cell, presenting opportunities for real-life applications. Additionally, the enhancement in the range of operational current density of the Ni-W cell compared to the Ni-F electrode depicts a four-fold improvement in the current density at the maximum operation point. These enhancements, owing to the presence of nanowires, demonstrate excellence in biofilm/electrode interface formation. The 1D structure of these nanowires penetrates the depth of the coated biofilm, and their metallic nature facilitates charge acquisition from substrate oxidation. Furthermore, mass transfer from the substrate to the anode electrode is improved, exhibiting better structural conformation alongside optimized feeding flow in the cell.

A comprehensive understanding of the cells' response to high and low current densities can be achieved through the polarization curves shown in Fig. 4b and e for the Ni-F and Ni-W MFCs, respectively. The presence of nickel silicide nanowires does not significantly impact the anode overpotential, as indicated by the minimal variation in OCP between the cells. The polarization curve can be divided into three regions: activation, ohmic, and concentration polarization<sup>61</sup>. Although activation losses at low current densities in the Ni-F anode are significant, causing a steep decline in cell potential, these losses are mitigated in the Ni-W electrode, which benefits from a higher surface area and improved biofilm formation. For instance, with a  $47 \text{ k}\Omega$  external resistance, the Ni-F electrode experiences a potential drop of 190 mV from OCP, whereas the Ni-W cell shows a reduced drop of 77 mV. This reduction in potential loss and the gentler initial slope for the Ni-W electrode suggests a lower activation energy required for electron extraction from the oxidized substrate<sup>62</sup>. At the optimal flow rate, the Ni-W cell exhibits a nearly linear response across current densities, with a broad ohmic region indicating consistent electron extraction from the oxidizing substrate. The lower slope of the ohmic overpotential in the Ni-W cell, compared to the Ni-F cell, highlights the pivotal role of nanowires in enhancing charge acquisition. Additionally, the potential drop across the operational range is limited to 383 mV in the Ni-W cell, compared



to 496 mV in the Ni-F cell, reflecting reduced internal resistance and improved charge attainment in the Ni-W MFC. The internal resistance can be determined from the ohmic region when there is a negligible increase in overpotentials<sup>63</sup>; for the Ni-W cell at the optimal flow rate, it is calculated to be 1.53 k $\Omega$ . This value can also be inferred using Jacobi's law, which expresses that maximum power generation occurs when the external resistance equals the internal resistance<sup>64</sup>. Analysis of the power density curves reveals a notable difference in the point of maximum power production: the Ni-W cell achieves optimal power at a lower external resistance compared to the Ni-F cell. For the Ni-F cell, the extremum occurs at an external resistance of 4.7 k $\Omega$  across all substrate flow rates. In contrast, the Ni-W cell shows varying maximum power values with different flow rates: at the optimal flow rate of 4  $\mu\text{l min}^{-1}$ , the ideal external resistance is 1 k $\Omega$ , while other flow rates tend to saturate at 2.2 k $\Omega$ . The higher internal resistance observed at other flow rates may result from high oxide byproducts and nutrient deficiencies at low flow rates, or mass transfer issues, shear stresses, and removal of electron transfer mediators at high flow rates. Considering either direct or indirect electron transfer mechanisms, both observed in *E. coli*<sup>65</sup>, whether through anaerobic respiration or electron shuttles like cytochrome c, require an optimal flow rate to facilitate effective electron transfer to the electrodes. The lower internal resistance at the optimal flow rate significantly enhances cell performance. The internal resistance values obtained from the polarization curve align with those predicted by Jacobi's law, reflecting the improved biofilm formation that contributes to the linear response characteristics of the Ni-W cell. Furthermore, the polarization curves also demonstrate improved mass transfer in the Ni-W cell. While the Ni-F cell shows a shift away from linear response at higher current densities, mass transport of substances to the nanowire-coated electrode is facilitated in the Ni-W cell and prohibits concentration losses in higher current densities.

The electrochemical behavior of both Ni-W and Ni-F anodes was investigated using electrochemical impedance spectroscopy. The experiment is conducted by introducing reference and counter electrodes into the substrate medium within the encapsulated cell, with the nickel-based anode serving as the working electrode. The Nyquist plots presented in Fig. 5a illustrate the distinct electrochemical characteristics of biofilm-covered bare and nanostructured electrodes. The EIS data for the Ni-F electrode exhibit an incomplete semicircle across the entire frequency range, with a predominant response in the low- to mid-frequency region. In contrast, the Ni-W electrode displays a distorted semicircle in the high-frequency region, followed by a broadened, incomplete arc in the low-frequency domain, indicative of both faradaic and non-faradaic processes. This double-arc configuration suggests the presence of an additional charge transfer pathway in the Ni-W electrode compared to bare nickel foam. The slow anaerobic respiration of *E. coli*, involving the oxidation of nutrients, is characterized by a high impedance, which is reflected in the low-frequency region of the bio-electrochemical activity<sup>66</sup>. The EIS data for the Ni-F electrode follows this charge transfer regime. The arc in the mid to high-

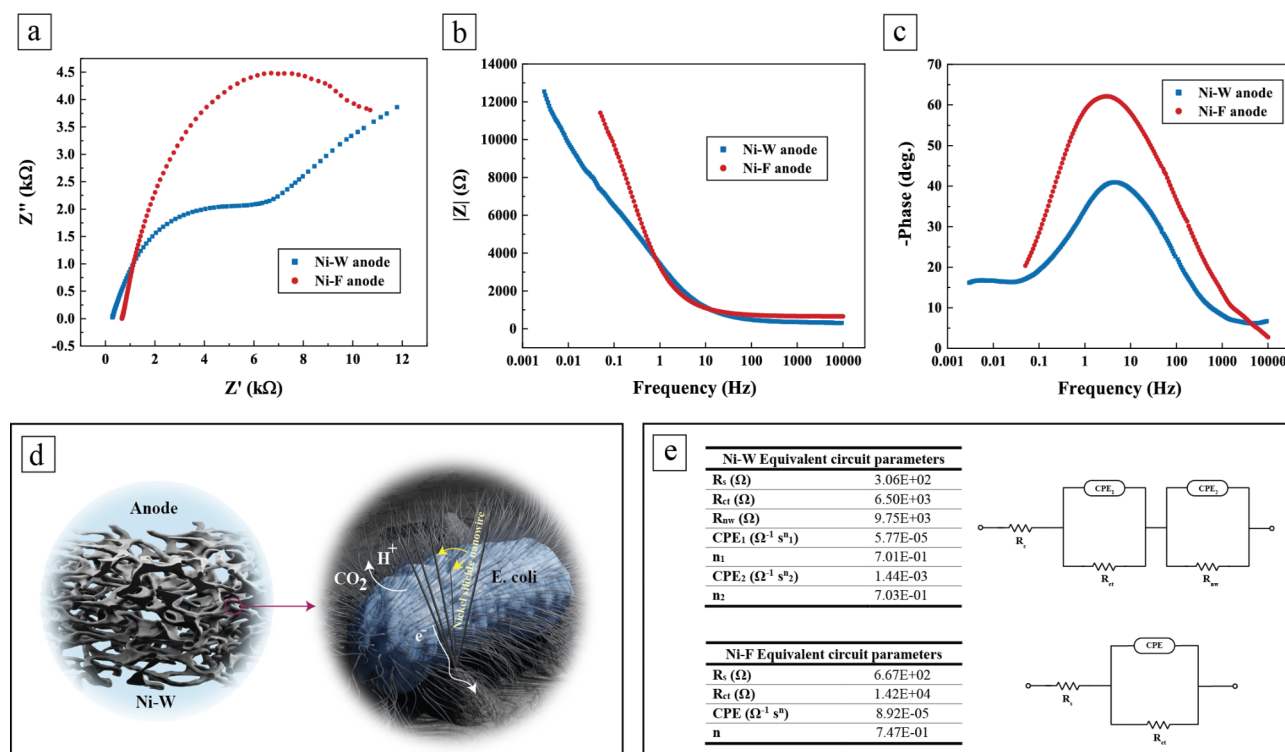


**Fig. 5.** Electrochemical investigation and charge transfer pathway of the Ni-F and Ni-W electrodes. (a) EIS Nyquist plot, and (b) and (c) Bode plots of bare and nickel silicide-covered nickel foams. (d) Schematic representation of the enhanced charge transfer pathway facilitated by bacterial inoculation on the nickel silicide nanowire-covered surface. (e) Equivalent circuit models and their corresponding parameters for Ni-F and Ni-W electrodes.



frequency range of the Nyquist plot is attributed to facilitated charge transfer from the electrolyte to the anode electrode. Ramasamy et al. have associated this behavior with the role of redox mediators and their shuttle redox processes<sup>67</sup>. Since the fabricated cell does not contain artificial mediators, the observed behavior is likely due to endogenous electron transfer pathways or enhanced charge transfer routes, potentially facilitated by the nanowires. This interpretation can be supported by the absence of the high frequency charge transfer regime in the Ni-F electrode's data. Furthermore, the secretion of redox mediators by *E. coli* is debated, and the role of membrane-bound cytochromes in the extracellular electron transfer pathway of this bacterium is considered significant<sup>68</sup>.

A more detailed analysis is provided by the Bode plots, shown in Fig. 5b and c. The phase plot across excitation frequencies reveals a dominant time constant in the mid-frequency region for the Ni-W electrode while the dominant phase shift in the Ni-F electrode occurs at lower frequencies. The predominance of faradaic processes in the Ni-W electrode suggests that the primary electron transfer mechanism occurs at higher frequencies, with byproducts of redox processes being mainly transferred to the anode electrode via facilitated routes. Considering the magnitude plot, the Ni-F electrode exhibits an abrupt transition from high to low magnitude, while this transition is more gradual for the nanostructured electrode, indicating an additional charge transfer route. This enhanced charge transfer is likely attributed to the presence of nanowires in the Ni-W electrode (Fig. 5d).

To further elucidate the role of nickel silicide nanostructures on the electrochemical behavior of the fabricated MFCs, the equivalent circuits and their corresponding parameters for both electrodes are presented in Fig. 5e. Both EIS data exhibit distorted semicircles revealing the non-ideal capacitive characteristics in the cells. This non-ideal capacitive behavior can be effectively modeled using a constant phase element (CPE) in the equivalent circuit of the cell which stems from distributed capacitive regions commonly seen in porous structures<sup>69,70</sup>. Although the Ni-F electrode provides a single dominant charge transfer pathway, the integration of nanostructures into a highly porous nickel foam in the Ni-W electrode introduces two distinct charge transfer pathways. The slow diffusion of charges towards the nickel foam surface contributes to the low-frequency response that dominates the Ni-F electrode, while the nickel silicide nanostructures facilitate the diffusion of bioactive molecules through the biofilm and their subsequent release into the flowing electrolyte. Accordingly, two distinct equivalent circuit models were obtained for the electrodes. Although the Randles circuit is commonly used for modeling MFCs<sup>71</sup>, diffusion limitations are more accurately represented by the R-CPE model rather than the finite Warburg element. The Ni-F electrode can be modeled using a series configuration comprising a solution resistance ( $R_s$ ) and a parallel R-C component, where the capacitive behavior is represented by constant phase elements. In contrast, the Ni-W electrode incorporates an additional charge transfer pathway attributed to the presence of nanostructures, necessitating an extra R-C configuration in series. The equivalent circuit parameters indicate enhanced charge transfer in the Ni-W electrode compared to bare nickel foam. The series resistance significantly decreases from 667  $\Omega$  to 306  $\Omega$ , highlighting the improved electron transport facilitated by the semi-metallic nanostructures.

#### *Effect of substrate type on power and current production*

The role of substrates as oxidizing agents in microorganism metabolism is highly considerable in microbial fuel cells<sup>72</sup>. The ability of bacteria to oxidize substrates and transfer electrons to the anode electrode dictates the current production capability of the cell. The impact of organic nutrients on bioelectricity production can be observed through the cellular respiration cycle and the efficiency of charge transfer through the electrolyte medium to the cell's electrodes. Additionally, substrates influence activation polarization by affecting the charge transfer mechanism at the electrolyte/electrode interface. Consequently, microbial organisms display varying performance depending on the feeding substrates provided. To investigate this, the performance of the Ni-W and Ni-F cells was evaluated using glucose and urea as substrates, as presented in Fig. 6. Glucose is commonly used in MFCs due to its role in the glycolysis pathway of cellular respiration, providing electrical charges through its oxidation. Also, the simultaneous production of bioelectricity and biodegradation of urea in the presence of *E. coli* bacteria has been reported<sup>73</sup>. Urea's significance lies in its presence as the primary component of human urine, making its use in MFCs promising for bio-implantable device applications.

The glucose feeding of *E. coli* bacteria introduces new hydraulic characteristics and alters the optimal flow rate for cell performance. As shown in Fig. 6a, the maximum power produced in both Ni-W and Ni-F cells occurs at a 2  $\mu\text{L min}^{-1}$  glucose feeding rate, representing a two-fold increase compared to a higher flow rate of 10  $\mu\text{L min}^{-1}$ . The power density and polarization curves of the glucose-fed cells at this optimal flow rate are presented in Fig. 6b. The open circuit potential of the cells differs between Ni-F and Ni-W electrodes, with latter showing enhancement over nutrient broth-fed cells. Considering the electrodes' overpotentials, the OCP value can be influenced by two redox reactions: one associated with nickel oxidation and the other with substrate oxidation, both affected by the choice of substrate<sup>62</sup>. Despite the advantages of OCP, the high initial slope of potential decrease in the Ni-W MFC indicates significant activation polarization, suggesting high energy loss during the redox reaction and charge extraction from the microbial medium to the solid electrode. This initial step is followed by higher resistivity ohmic characteristics in the cell, compared to the nutrient broth-fed cell, resulting in reduced power production capability in both Ni-F and Ni-W MFCs. The 2.5-fold decrease in power generation highlights the role of nutrient broth as a substrate in the MFC's operation. The maximum power of 133  $\text{mW m}^{-2}$  is achieved with an external resistive load of 4.7  $\text{k}\Omega$ , indicating higher internal resistance due to the glucose medium. This can be attributed to the reduced redox reactions in microbial metabolism with glucose, leading to a four-fold decrease in current generation capability. Additionally, the cell experienced electrical depletion, evidenced by a potential overshoot in the power density plot when decreasing the external resistance from 2.2  $\text{k}\Omega$  to 1  $\text{k}\Omega$ . This overshoot indicates the cell's inability to generate the required electrons through substrate oxidation and ionic depletion at lower external resistances<sup>74</sup>. Although this could result from insufficient acclimation of bacteria to the external resistance, adequate time was provided at each measurement step to ensure stable electrical

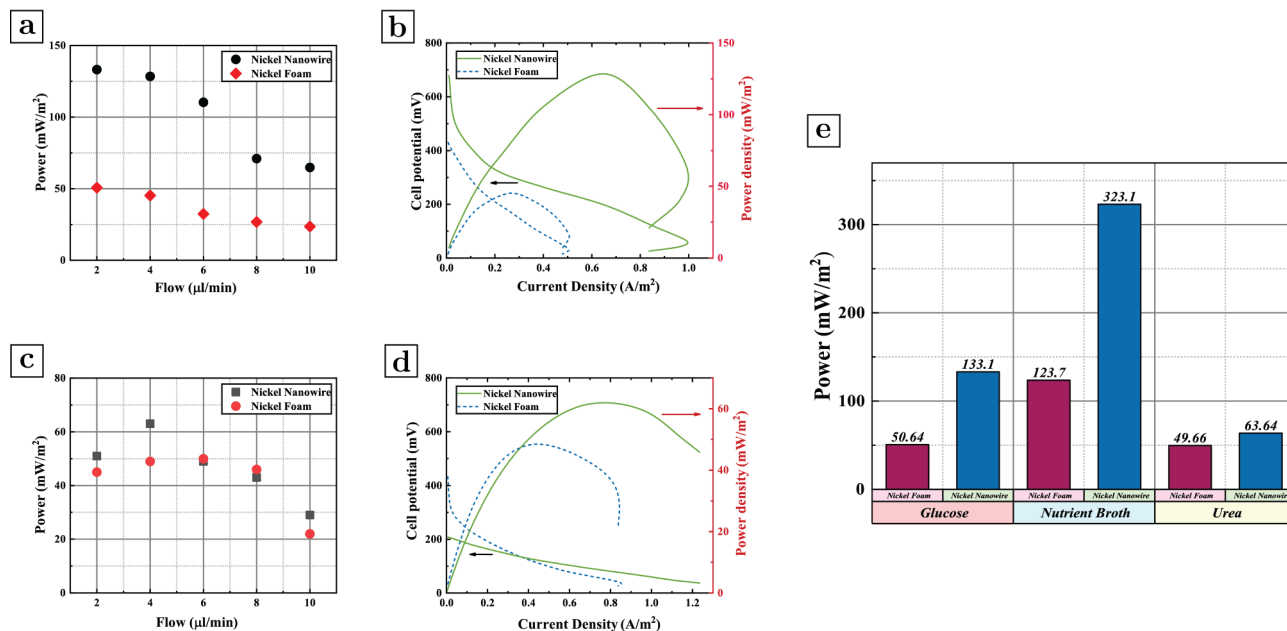


**Fig. 6.** Effect of different substrate types on power and current production. **(a)** Maximum surface power density of nickel silicide nanowires on foam at various flow rates using glucose as the microbial substrate. **(b)** Surface power density and polarization curve of nickel silicide nanowires on foam at the optimal glucose flow rate ( $2 \mu\text{L min}^{-1}$ ). **(c)** Maximum surface power density of nickel silicide nanowires on foam at various flow rates using urea as the microbial substrate. **(d)** Surface power density and polarization curve of nickel silicide nanowires on foam at the optimal urea flow rate ( $4 \mu\text{L min}^{-1}$ ). **(e)** Comparison of the maximum surface power density of nickel foam versus nickel silicide nanowires on foam with different feeding substrates.

characteristics. The overshoot phenomenon may arise from various factors, including insufficient redox agents for charge generation<sup>75</sup> and inadequate feeding rates<sup>76</sup>. The lower electroactivity of microorganisms in glucose oxidation has limited current generation, reducing the current density at maximum power to  $650 \text{ mA m}^{-2}$ , which negatively impacts the higher current activity compared to the nutrient broth-fed cell.

The microbial activities of Ni-F and Ni-W cells with urea as the substrate are presented in Fig. 6c and d. The maximum power density is achieved at a flow rate of  $4 \mu\text{L min}^{-1}$ , showing a decrease in power generation compared to cells fed with nutrient broth and glucose. The underlying cause of this underperformance can be traced in the polarization curve of the cell (Fig. 6d). Although the nickel foam maintains its functionality in the urea environment and exhibits comparable power production performance to glucose feeding, the nanostructure-coated surface displays a significant decrease in open circuit potential and increased electrode overpotential. The high electrode overpotential in the nanowire MFC indicates structural deterioration of the electrode surface. This phenomenon may be attributed to the potential urea etching of the nickel silicide structures, leading to the dissolution of nickel silicide into urea and the subsequent formation of hydroxide nanostructures<sup>77</sup>. These sequential reactions result in substantial deformation of the anode and adversely affect the cell's power generation performance. Despite the high activation overpotential required for the nickel foam/urea charge exchange, the nanostructured cell shows a linear response across current densities, offering sustainable performance even with lower power generation capability. This results in higher current density generation in the urea-fed cell compared to glucose, although it remains lower than that achieved with nutrient broth substrate oxidation.

The power production performance of Ni-W and Ni-F cells under three nutrient-feeding conditions is depicted in Fig. 6e. Comparing these substrates, nutrient broth demonstrates superior results in both anodic configurations relative to glucose and urea. Although glucose is widely used as an oxidizing agent in microbial fuel cells, the use of a culture medium, specifically nutrient broth, enhances the performance of the microbial fuel cell. Besides the desirable growth environment provided by the culture medium, the chemical composition of nutrient broth contributes to its superior performance in MFCs. While beef extract and peptone do not significantly contribute to the bioelectrical activity of the cell, yeast extract plays a notable role. Yeast cells have been solely utilized as biocatalysts in MFCs<sup>78</sup> and have also been proposed as exogenous mediators in yeast-based MFCs to enhance redox product transfer to the electrodes<sup>47</sup>. Additionally, NaCl in the nutrient broth enhances the charge transfer capability of the electrolyte and reduces the ohmic resistance of the cell. Therefore, nutrient broth presents itself as a favorable substrate for microbial fuel cells. In comparison, urea and glucose exhibit similar performance in nickel-based cells, although urea-fed cells show slightly better current generation. This can be attributed to the conductivity of these solutions. Glucose, being a non-electrolyte, lacks free ions, whereas urea, although exhibiting low electrical conductivity, is still effective in charge transfer. However, despite

Anode material	Cathode material	$P_{\max}$ (mW $m^{-2}$ )	$P_{\max}$ (W $m^{-3}$ )	$I_{\max@P_{\max}}$ (A $m^{-2}$ )	Biocatalyst	Chamber configuration	Substrate	Ref.
Ni-W	Carbon cloth	323.1	923	2.24	Escherichia coli	Single	NB	This work
Ni-F	Carbon cloth	123.7	353	0.64	Escherichia coli	Single	NB	This work
Graphene-Nickel foam	Carbon paper	1110	-	2.15	Mixed	Dual	Sodium acetate in PBS (anolyte) Ferricyanide in PBS (catholyte)	44
Graphene-Nickel foam	-	3903	-	18	Shewanella putrefaciens	Dual	LB (anolyte) Ferricyanide in PBS (catholyte)	45
3D Graphene-Nickel foam	Carbon cloth	-	661	2.2	Shewanella oneidensis	Dual	TSB (anolyte) Ferricyanide in PBS (catholyte)	13
Nickel nanostructured-Nickel foil	Carbon cloth	58	343	0.4	Escherichia coli	Single	NB	5
Nickel plate	Carbon cloth	-	104	0.11	Escherichia coli	Single	NB	73
Ni-carbon felt	Carbon felt	130.72	-	0.76	Mixed	Dual	Wastewater (anolyte) ammonium chloride in YPD (catholyte)	46
NiO-graphene/Nickel foam	Carbon cloth	3632	-	17.5	Shewanella putrefaciens	Dual	LB (anolyte) Ferricyanide in PBS (catholyte)	80

**Table 1.** Comparison of nickel-based microbial fuel cells. \*NB, Nutrient broth; LB, Lysogeny broth; TSB, Trypticase soy broth; YPD, yeast extract peptone dextrose.

the advantages of urea, its incompatibility with nickel silicide results in a deterioration of cell performance, making it an unsuitable feedstock for these cells.

#### Comparison of maximum power densities in nickel-based MFCs

The power density and current generation capabilities of the fabricated cells are brought into comparison with other reported nickel-based microbial fuel cells, as shown in Table 1. The Ni-W cell exhibits the highest reported maximum power density among nutrient broth-fed fuel cells. Additionally, the nanowire-coated electrodes offer a three-fold enhancement in power density compared to the best-reported glucose-fed fuel cells<sup>73</sup>. When compared with microfluidic-based MFCs with nickel electrodes reported in<sup>73</sup>, our Ni-W cell shows significant improvements across all three feeding substrates used with *E. coli* which is similarly used in both studies. This advantage is attributed to the nickel silicide nanostructures incorporated into the nickel foam. The semi-metallic nature of these nanostructures facilitates electron transfer to the external circuit, which is a major factor in the high-power density and current generation. Furthermore, the 3D scaffold prepared by covering nickel foams with nanostructures effectively reduces mass transport limitations and deploys better microbial colonization and biofilm formation. This structural design results in improved charge transfer capabilities and higher power and current generation, making it highly efficient.

The cell's sustained performance at high current densities supports this claim. The ability to maintain high current density across a wide range of resistive loads is due to the efficient nanostructure of the nickel foam. Compared to our previously reported cells with nickel foam/nickel nanostructure configurations<sup>5</sup>, the growth of nickel silicide on the nickel foam demonstrates a three-fold enhancement in surface power density production.

Fabricating 3D structures has been established as an effective method for enhancing the power production capability of microbial fuel cells<sup>8</sup>. In this study, we have introduced nickel silicide on nickel foam, resulting in improved power and current generation performance in both nutrient broth and glucose-based MFCs. Although other modifications, such as graphene coatings, have demonstrated higher power generation efficiency, there are significant concerns associated with incorporating 2D and 1D carbon-based structures into MFCs. Beyond the higher end-product costs of these materials comparing metal-based electrodes due to their significant conductivity shortages<sup>79</sup>, the biocompatibility issues in utilizing them as MFC anode is a significant concern<sup>48,49</sup>.

Additionally, the Ni-W cell's performance in *Escherichia coli*-based setups with nutrient broth and other substrates demonstrates its versatility. The ability to use a wide range of substrates with similar microbial species is crucial for the scalability of MFCs. The Ni-W cell's design also allows for better deployment in real-world environments, where varying conditions and substrates are used for microbial power generation. In contrast, many other cells using advanced materials like graphene or carbon-based electrodes may struggle with scalability due to the high costs or challenges in microbial interaction.

Overall, our proposed strategy has shown promising results in microbial fuel cell fabrication. While further improvements are needed, it offers a reliable platform for advancing the practical application of micro-sized power-generating microbial fuel cells.

## Conclusion

In summary, the introduction of nickel silicide nanowires in microbial fuel cell technology significantly enhanced the power generation capabilities of nickel-based electrodes. This study demonstrates a novel and facile synthesis approach for these nanostructures using a low-pressure chemical vapor deposition technique. The sequential process, utilizing silane and ammonia gaseous precursors, provided a confined region for one-dimensional nanowire growth. The restricted silicon nitride regions, achieved through the catalytic decomposition of



ammonia on the nickel surface and its subsequent reaction with a silicon-containing precursor, facilitated the interdiffusion of nickel atoms and the elongated growth of nickel silicide nanostructures. Comparing the ammonia-free medium with our proposed growth protocol, the role of the nitrogen-containing precursor was assessed by the suppression of one-dimensional growth.

The nanostructured 3D configuration, resulting from the growth of nickel silicide nanowires on nickel foam, exhibited delicate structural characteristics conducive to microbial inoculation and biofilm formation in MFCs. The presence of nickel silicide nanostructures as the anode in fabricated MFCs resulted in a 2.5-fold increase in power generation and a 4-fold increase in achievable current density compared to bare nickel foam, achieving a peak power density of 323 mW m<sup>-2</sup> and a current density of 2.4 A m<sup>-2</sup> under optimal conditions. These advantages were due to the semi-metal nature of the nanowires, which facilitated charge transfer to the external circuit, and the structural enhancement, which provided a more suitable pathway for charge extraction at the electrode/electrolyte interface. These facilitated charge transfer routes in the fabricated cell were evident in EIS studies, showing mid-to-high frequency charge transfer in the microbial microenvironment. Additionally, anchoring nickel foam with nickel silicide nanowires provided sustainable power generation at high current densities, highlighting the role of these nanostructures in enhancing charge transfer in the fabricated cell. Incorporating these features in the microfluidics configuration enabled power densities up to 923 W m<sup>-3</sup> in our fabricated MFC. Comparing various electroactive substrates for cell performance optimization, nutrient broth exhibited a significant advantage over glucose and urea substrates, making it the best choice for nickel-based MFCs. The nanowire-enriched 3D electrode demonstrated sustainable power generation performance at high current densities with minimal 7% variation in the range of 1.5 to 2.7 A m<sup>-2</sup>, reflecting the facilitated charge acquisition routes provided by the preferable interaction of the electrode and microbial biofilm with the redox substrate. These results highlight the potential of nickel silicide nanowires in energy harvesting applications from microbial environments. The facile synthesis of the presented nanostructured 3D configuration through anchoring nickel foam with nickel silicide nanowires offers a robust platform for further enhancements and applications in MFC technology.

### Data availability

All the data analyzed and presented in this study are available from the corresponding author upon reasonable request.

Received: 28 December 2024; Accepted: 24 February 2025

Published online: 05 March 2025

### References

- Cai, W., Liu, W., Han, J. & Wang, A. Enhanced hydrogen production in microbial electrolysis cell with 3D self-assembly nickel foam-graphene cathode. *Biosens. Bioelectron.* **80**, 118–122 (2016).
- Luo, H., Xu, P., Roane, T. M., Jenkins, P. E. & Ren, Z. Microbial desalination cells for improved performance in wastewater treatment, electricity production, and desalination. *Bioresour Technol.* **105**, 60–66 (2012).
- Gude, V. G. Wastewater treatment in microbial fuel cells – an overview. *J. Clean. Prod.* **122**, 287–307 (2016).
- Jiang, Y. et al. A novel microbial fuel cell sensor with Biocathode sensing element. *Biosens. Bioelectron.* **94**, 344–350 (2017).
- Mousavi, M. R. et al. Improvement of the microfluidic microbial fuel cell using a nickel nanostructured electrode and microchannel modifications. *J. Power Sources* **437**, 226891 (2019).
- Gao, Y., Mohammadifar, M. & Choi, S. From microbial fuel cells to biobatteries: moving toward On-Demand micropower generation for Small-Scale Single-Use applications. *Adv. Mater. Technol.* **4**, 1900079 (2019).
- Logan, B. E. et al. Assessment of microbial fuel cell configurations and power densities. *Environ. Sci. Technol. Lett.* **2**, 206–214 (2015).
- Sonawane, J. M., Yadav, A., Ghosh, P. C. & Adeloju, S. B. Recent advances in the development and utilization of modern anode materials for high performance microbial fuel cells. *Biosens. Bioelectron.* **90**, 558–576 (2017).
- Abbas, A. A., Farrag, H. H. & El-Sawy, E. Allam, N. K. Microbial fuel cells with enhanced bacterial catalytic activity and stability using 3D nanoporous stainless steel anode. *J. Clean. Prod.* **285**, 124816 (2021).
- Chong, P., Erable, B. & Bergel, A. Effect of pore size on the current produced by 3-dimensional porous microbial Anodes: A critical review. *Bioresour Technol.* **289**, 121641 (2019).
- Liu, J. et al. Graphene/carbon cloth anode for high-performance mediatorless microbial fuel cells. *Bioresour Technol.* **114**, 275–280 (2012).
- Jiang, H., Yang, L., Deng, W., Tan, Y. & Xie, Q. Macroporous graphitic carbon foam decorated with polydopamine as a high-performance anode for microbial fuel cell. *J. Power Sources* **363**, 27–33 (2017).
- Wang, H. et al. High power density microbial fuel cell with flexible 3D graphene–nickel foam as anode. *Nanoscale* **5**, 10283–10290 (2013).
- Wu, G. et al. Polypyrrole/sargassum activated carbon modified stainless-steel sponge as high-performance and low-cost Bioanode for microbial fuel cells. *J. Power Sources* **384**, 86–92 (2018).
- Wang, R. et al. FeS<sub>2</sub> nanoparticles decorated graphene as microbial-fuel-cell anode achieving high power density. *Adv. Mater.* **30**, 1800618 (2018).
- Yuan, H. & He, Z. Graphene-modified electrodes for enhancing the performance of microbial fuel cells. *Nanoscale* **7**, 7022–7029 (2015).
- Manickam, S. S. et al. Activated carbon nanofiber anodes for microbial fuel cells. *Carbon* **53**, 19–28 (2013).
- Thepsarungsikul, N., Ng, T., Lefebvre, O. & Ng, H. Different types of carbon nanotube-based anodes to improve microbial fuel cell performance. *Water Sci. Technol.* **69**, 1900–1910 (2014).
- Higgins, S. R. et al. Fabrication of macroporous Chitosan scaffolds doped with carbon nanotubes and their characterization in microbial fuel cell operation. *Enzyme Microb. Technol.* **48**, 458–465 (2011).
- Wei, J., Liang, P. & Huang, X. Recent progress in electrodes for microbial fuel cells. *Bioresour Technol.* **102**, 9335–9344 (2011).
- Banerjee, A., Calay, R. K. & Mustafa, M. Review on material and design of anode for microbial fuel cell. *Energies* **15**, 2283 (2022).
- Kaur, R., Marwaha, A., Chhabra, V. A., Kim, K. H. & Tripathi, S. K. Recent developments on functional nanomaterial-based electrodes for microbial fuel cells. *Renew. Sustain. Energy Rev.* **119**, 109551 (2020).
- Ma, J. et al. Progress on anodic modification materials and future development directions in microbial fuel cells. *J. Power Sources* **556**, 232486 (2023).

24. Santos, J. S., Tarek, M., Sikora, M. S., Praserthdam, S. & Praserthdam, P. Anodized TiO<sub>2</sub> nanotubes arrays as microbial fuel cell (MFC) electrodes for wastewater treatment: an overview. *J. Power Sources* **564**, 232872 (2023).
25. Liu, Y., Zhang, X., Zhang, Q. & Li, C. Microbial fuel cells: nanomaterials based on anode and their application. *Energy Technol.* **8**, 2000206 (2020).
26. Yaqoob, A. A. et al. Recent advances in anodes for microbial fuel cells: an overview. *Materials* **13**, 2078 (2020).
27. Baudler, A., Schmidt, I., Langner, M., Greiner, A. & Schröder, U. Does it have to be carbon? Metal anodes in microbial fuel cells and related bioelectrochemical systems. *Energy Environ. Sci.* **8**, 2048–2055 (2015).
28. Dumas, C. et al. Checking graphite and stainless anodes with an experimental model of marine microbial fuel cell. *Bioresour Technol.* **99**, 8887–8894 (2008).
29. Cai, T. et al. Application of advanced anodes in microbial fuel cells for power generation: A review. *Chemosphere* **248**, 125985 (2020).
30. Hosseini, M. et al. Highly crystalline nickel silicon sheets on silicon substrates using hydrogen plasma treatment. *Phys. Status Solidi (RRL) – Rapid Res. Lett.* **14**, 1900404 (2020).
31. Pandey, R. K., Maity, G., Pathak, S., Kalita, P. & Dubey, S. New insights on Ni-Si system for microelectronics applications. *Microelectron. Eng.* **264**, 111871 (2022).
32. Hosseini, M. & Mohajerzadeh, S. Evolution of silicon-Nickel nanosheets on (111) silicon substrates to realize reduced graphene Oxide-Silicide heterostructures. *IEEE Electron. Device Lett.* **40**, 1690–1693 (2019).
33. Schmitt, A. L., Higgins, J. M., Szczech, J. R. & Jin, S. Synthesis and applications of metal silicide nanowires. *J. Mater. Chem.* **20**, 223–235 (2010).
34. Chen, L. J. & Wu, W. W. Metal silicide nanowires. *Jpn J. Appl. Phys.* **54**, 07JA04 (2015).
35. Decker, C., Solanki, R., Freeouf, J., Carruthers, J. & Evans, D. Directed growth of nickel silicide nanowires. *Appl. Phys. Lett.* **84**, 1389–1391 (2004).
36. Dasgupta, N. P. et al. Nickel silicide nanowire arrays for Anti-Reflective electrodes in photovoltaics. *Adv. Funct. Mater.* **22**, 3650–3657 (2012).
37. Iriarte, G. Growth of nickel disilicide nanowires by CVD. *J. Non-Cryst Solids.* **356**, 1135–1144 (2010).
38. Gharooni, M. et al. Realization of highly crystallographic three-dimensional nanosheets by a stress-induced oriented-diffusion method. *Appl. Phys. Lett.* **105** (2014).
39. Szczech, J. R., Schmitt, A. L., Bierman, M. J. & Jin, S. Single-crystal semiconducting chromium disilicide nanowires synthesized via chemical vapor transport. *Chem. Mater.* **19**, 3238–3243 (2007).
40. Liu, B., Wang, Y., Dilts, S., Mayer, T. S. & Mohny, S. E. Silicidation of silicon nanowires by platinum. *Nano Lett.* **7**, 818–824 (2007).
41. Kim, J., Bae, J. U., Anderson, W. A., Kim, H. M. & Kim, K. B. Solid-state growth of nickel silicide nanowire by the metal-induced growth method. *J. Mater. Res.* **21**, 2936–2940 (2006).
42. Du, N., Fan, X., Yu, J., Zhang, H. & Yang, D. Ni<sub>3</sub>Si<sub>2</sub>-Si nanowires on Ni foam as a high-performance anode of Li-ion batteries. *Electrochem. Commun.* **13**, 1443–1446 (2011).
43. Jiang, Y., Li, Z., Li, B., Zhang, J. & Niu, C. Ni<sub>3</sub>Si<sub>2</sub> nanowires grown in situ on Ni foam for high-performance supercapacitors. *J. Power Sources* **320**, 13–19 (2016).
44. Yang, Y. et al. Boosting power density of microfluidic biofuel cell with porous three-dimensional graphene@nickel foam as flow-through anode. *Int. J. Hydrogen Energy* **43**, 18516–18520 (2018).
45. Qiao, Y., Wu, X. S., Ma, C. X., He, H. & Li, C. M. A hierarchical porous graphene/nickel anode that simultaneously boosts the bio- and electro-catalysis for high-performance microbial fuel cells. *RSC Adv.* **4**, 21788–21793 (2014).
46. Mahmoodzadeh, F., Navidjouy, N., Alizadeh, S. & Rahimnejad, M. Investigation of microbial fuel cell performance based on the nickel thin film modified electrodes. *Sci. Rep.* **13**, 20755 (2023).
47. Sayed, E. T., Barakat, N. A. M., Abdelkareem, M. A., Fouad, H. & Nakagawa, N. Yeast extract as an effective and safe mediator for the Baker's-Yeast-Based microbial fuel cell. *Ind. Eng. Chem. Res.* **54**, 3116–3122 (2015).
48. Ou, L. et al. Toxicity of graphene-family nanoparticles: a general review of the origins and mechanisms. *Part. Fibre Toxicol.* **13**, 57 (2016).
49. Liu, Y., Zhao, Y., Sun, B. & Chen, C. Understanding the toxicity of carbon nanotubes. *Acc. Chem. Res.* **46**, 702–713 (2013).
50. Peter, A. P. et al. Phase formation and morphology of nickel silicide thin films synthesized by catalyzed chemical vapor reaction of nickel with silane. *Chem. Mater.* **27**, 245–254 (2015).
51. Wang, Y. & Sibener, S. J. Reactive deposition of silicon nanowires templated on a stepped nickel surface. *J. Phys. Chem. B* **106**, 12856–12859 (2002).
52. Lindroos, J. et al. Nickel: A very fast diffuser in silicon. *J. Appl. Phys.* **113** (2013).
53. Fan, X., Zhang, H., Du, N. & Yang, D. Phase-controlled synthesis of nickel silicide nanostructures. *Mater. Res. Bull.* **47**, 3797–3803 (2012).
54. Lucentini, I., Garcia, X., Vendrell, X. & Llorca, J. Review of the decomposition of Ammonia to generate hydrogen. *Ind. Eng. Chem. Res.* **60**, 18560–18611 (2021).
55. Zhang, L., Zhu, X., Li, J., Liao, Q. & Ye, D. Biofilm formation and electricity generation of a microbial fuel cell started up under different external resistances. *J. Power Sources* **196**, 6029–6035 (2011).
56. Rabaey, K. & Verstraete, W. Microbial fuel cells: novel biotechnology for energy generation. *Trends Biotechnol.* **23**, 291–298 (2005).
57. Ye, D. et al. Performance of a microfluidic microbial fuel cell based on graphite electrodes. *Int. J. Hydrogen Energy* **38**, 15710–15715 (2013).
58. Choban, E. R., Markoski, L. J., Wieckowski, A. & Kenis, P. J. A. Microfluidic fuel cell based on laminar flow. *J. Power Sources* **128**, 54–60 (2004).
59. Palanisamy, G. et al. A comprehensive review on microbial fuel cell technologies: processes, utilization, and advanced developments in electrodes and membranes. *J. Clean. Prod.* **221**, 598–621 (2019).
60. Karimi Alavijeh, M., Mardanpour, M. M. & Yaghmaei, S. A generalized model for complex wastewater treatment with simultaneous bioenergy production using the microbial electrochemical cell. *Electrochim. Acta* **167**, 84–96 (2015).
61. Logan, B. E. et al. Microbial fuel cells: methodology and technology. *Environ. Sci. Technol.* **40**, 5181–5192 (2006).
62. Shirkosh, M., Hojjat, Y. & Mardanpour, M. M. Boosting microfluidic microbial fuel cells performance via investigating electron transfer mechanisms, metal-based electrodes, and magnetic field effect. *Sci. Rep.* **12**, 7417 (2022).
63. Clauwaert, P. et al. Minimizing losses in bio-electrochemical systems: the road to applications. *Appl. Microbiol. Biotechnol.* **79**, 901–913 (2008).
64. Potrykus, S., León-Fernández, L. F., Nieznański, J., Karkosiński, D. & Fernandez-Morales, F. J. The influence of external load on the performance of microbial fuel cells. *Energies* **14** (2021).
65. Yoon, Y., Aziz, A. A., Chang, I. S. & Kim, B. Prevalence of Escherichia coli in electrogenic biofilm on activated carbon in microbial fuel cell. *Appl. Microbiol. Biotechnol.* **108**, 52 (2024).
66. Wang, H. et al. Electrochemical impedance spectroscopy applied to microbial fuel cells: A review. *Front. Microbiol.* **13** (2022).
67. Ramasamy, R. P., Gadhamshetty, V., Nadeau, L. J. & Johnson, G. R. Impedance spectroscopy as a tool for non-intrusive detection of extracellular mediators in microbial fuel cells. *Biotechnol. Bioeng.* **104**, 882–891 (2009).
68. Mouhib, M., Reggente, M., Li, L., Schuergers, N. & Boghossian, A. A. Extracellular electron transfer pathways to enhance the electroactivity of modified Escherichia coli. *Joule* **7**, 2092–2106 (2023).

69. Ramasamy, R. P., Ren, Z., Mench, M. M. & Regan, J. M. Impact of initial biofilm growth on the anode impedance of microbial fuel cells. *Biotechnol. Bioeng.* **101**, 101–108 (2008).
70. Orazem, M. E., Shukla, P. & Membrino, M. A. Extension of the measurement model approach for Deconvolution of underlying distributions for impedance measurements. *Electrochim. Acta* **47**, 2027–2034 (2002).
71. Kashyap, D. et al. Application of electrochemical impedance spectroscopy in bio-fuel cell characterization: A review. *Int. J. Hydrogen Energy* **39**, 20159–20170 (2014).
72. Pant, D., Van Bogaert, G., Diels, L. & Vanbroekhoven, K. A review of the substrates used in microbial fuel cells (MFCs) for sustainable energy production. *Bioresour Technol.* **101**, 1533–1543 (2010).
73. Mardanpour, M. M. & Yaghmaei, S. Characterization of a microfluidic microbial fuel cell as a power generator based on a nickel electrode. *Biosens. Bioelectron.* **79**, 327–333 (2016).
74. Ieropoulos, I., Winfield, J. & Greenman, J. Effects of flow-rate, inoculum and time on the internal resistance of microbial fuel cells. *Bioresour Technol.* **101**, 3520–3525 (2010).
75. Hong, Y., Call, D. F., Werner, C. M. & Logan, B. E. Adaptation to high current using low external resistances eliminates power overshoot in microbial fuel cells. *Biosens. Bioelectron.* **28**, 71–76 (2011).
76. Winfield, J., Ieropoulos, I., Greenman, J. & Dennis, J. The overshoot phenomenon as a function of internal resistance in microbial fuel cells. *Bioelectrochemistry* **81**, 22–27 (2011).
77. Ning, J. et al. Superior pseudocapacitive storage of a novel Ni<sub>3</sub>Si<sub>2</sub>/NiOOH/Graphene nanostructure for an All-Solid-State supercapacitor. *Nanomicro Lett.* **13**, 2 (2020).
78. Enas Taha, S. & Mohammad Ali, A. in *Old Yeasts* (eds Lucas Candida & Pais Celia) Ch. 3. (IntechOpen, 2017).
79. Li, S., Cheng, C. & Thomas, A. Carbon-Based Microbial-Fuel-Cell electrodes: from conductive supports to active catalysts. *Adv. Mater.* **29**, 1602547 (2017).
80. Wu, X., Shi, Z., Zou, L., Li, C. M. & Qiao, Y. Pectin assisted one-pot synthesis of three dimensional porous NiO/graphene composite for enhanced bioelectrocatalysis in microbial fuel cells. *J. Power Sources* **378**, 119–124 (2018).

## Acknowledgements

This research did not receive any specific grant from funding agencies in the public, commercial, or non-for-profit sectors.

## Author contributions

Conceptualization: MH, SAE, MRM, SM; Methodology: MH, SAE, MRM, MJ, MA; Investigation: MH, SAE, MRM, MJ; Visualization: MH, SAE; Supervision: SM, ZS; Writing-original draft: MH, SAE; Writing-review & editing: MH, SAE, SM.

## Declarations

### Competing interests

The authors declare no competing interests.

### Additional information

**Correspondence** and requests for materials should be addressed to S.M.

**Reprints and permissions information** is available at [www.nature.com/reprints](http://www.nature.com/reprints).

**Publisher's note** Springer Nature remains neutral with regard to jurisdictional claims in published maps and institutional affiliations.

**Open Access** This article is licensed under a Creative Commons Attribution-NonCommercial-NoDerivatives 4.0 International License, which permits any non-commercial use, sharing, distribution and reproduction in any medium or format, as long as you give appropriate credit to the original author(s) and the source, provide a link to the Creative Commons licence, and indicate if you modified the licensed material. You do not have permission under this licence to share adapted material derived from this article or parts of it. The images or other third party material in this article are included in the article's Creative Commons licence, unless indicated otherwise in a credit line to the material. If material is not included in the article's Creative Commons licence and your intended use is not permitted by statutory regulation or exceeds the permitted use, you will need to obtain permission directly from the copyright holder. To view a copy of this licence, visit <http://creativecommons.org/licenses/by-nc-nd/4.0/>.

© The Author(s) 2025